Evolution of oxygen and stratification in the North Pacific Ocean in CMIP6 Earth System Models

Lyuba Novi[1], Annalisa Bracco[1], Takamitsu Ito[1], Yohei Takano[2,3]

[1]School of earth and Atmospheric Sciences,Georgia Institute of technology , Atlanta, GA, USA.
5   [2]British Antarctic Survey, Cambridge, UK.
[3]Los Alamos National Laboratory, Los Alamos, NM, USA.

Correspondence to: L. Novi (lnovi3@gatech.edu)

Abstract. This study examines the linkages between the upper ocean (0-200 m) oxygen (O_2) content and stratification in the
10 North Pacific Ocean in four Earth system models (ESMs), an ocean hindcast simulation, and ocean reanalysis data. Trend
and variability of oceanic O_2 content are driven by the imbalance between physical supply and biological demand. The
physical supply is primarily controlled by ocean ventilation, which is responsible for the transport of O_2-rich surface waters
into subsurface. To quantify the ocean ventilation, Isopycnic Potential Vorticity (IPV) is used as a dynamical proxy in this
study. IPV is a quasi-conservative tracer proportional to density stratification, which can be interpreted as a proxy for ocean
15 ventilation and can be evaluated from temperature and salinity measurements alone. The predictability potential of the IPV
field is evaluated through its information entropy. Results highlight a strong O_2-IPV connection and somewhat higher (than
in rest of the basin) predictability potential for IPV in the tropical Pacific, in the area strongly affected by the El Niño
Southern Oscillation. This pattern of higher predictability and strong anticorrelation between O_2 and stratification is robust
across multiple models and datasets. In contrast, the variability of IPV at mid-latitudes has low predictability potential and its
20 center of action differs from that of O_2. In addition, the locations of extreme events or hotspots may or may not differ among
the two fields, with a strong model dependency, which persists in future projections. These results, on one hand, suggest the
possibility to monitor ocean O_2 through few observational sites co-located with some of the more abundant IPV
measurements in the tropical Pacific, and, on the other, question the robustness of the IPV-O_2 relationship in the extra-
tropics. The proposed framework helps characterizing and interpreting O_2 variability in relation to physical variability and
25 may be especially useful in the analysis of new observationally-based data products derived from the BGC-ARGO float
array in combination with the traditional but far more abundant ARGO data.

1 Introduction

Dissolved oxygen (O_2) in the oceans is crucial for biogeochemical cycling, marine ecosystem and redox chemistry of
seawater. O_2 is a key element for the survival and functioning of marine organisms as fish, shellfish, marine mammals, and
30 other aquatic life rely on O_2 to breathe and carry out essential metabolic processes. Many commercially important fish

species and shellfish thrive only on well-oxygenated waters. Growth, reproduction, and overall health of marine organisms depends on the balance between metabolic demands and O_2 supply (Deutsch et al., 2015).

Ocean deoxygenation refers to the long-term decrease in the concentration of O_2 in the Earth's oceans. At the global scale, the O_2 inventory has been declining significantly over the past decades according to historical observations (Ito et al., 2017;

35   Schmidtko et al., 2017). Changes in O_2 concentrations can reflect the impacts of climate change, nutrient pollution, eutrophication, and other human-induced stressors. Monitoring ocean oxygen levels helps scientists assessing the health and resilience of marine ecosystems and identifying areas that may be prone to O_2 depletion or hypoxic events. Monitoring and predicting oxygen levels in the oceans is especially important around and within Oxygen Minimum Zones (OMZs), which are characterized by layers in the water column with very low O_2 concentration due to biological, chemical, and physical

40   processes. As oceans warm, OMZs are posed to increase in number and size across the globe. In the North Pacific, a large OMZ exists on the eastern side of the tropical Pacific, and its variability and trends are important also for nitrogen cycling and production of N_2O, a potent greenhouse gas (Nevison et al., 2003; Yang et al., 2017).

Interpreting changes in O_2 concentrations requires understandings in ocean circulation, mixing, air-sea gas transfer, biological productivity and respiration. The air-sea gas exchange for O_2 is relatively efficient, and it maintains the surface

45   water close to saturation with the overlying atmosphere for ice-free regions. Ocean circulation is the primary pathway through which O_2 is supplied (or ventilated) into the thermocline and deep ocean. In the subsurface, O_2 is gradually consumed by respiration due to the decomposition of dissolved and particulate organic matter. The O_2 concentration progressively decreases as water masses age. At climatological timescale, the rates of O_2 supply and consumption are balanced to sustain a steady state. In another words, changes in O_2 concentration are caused by an imbalance between O_2

50   supply and O_2 consumption.

On the supply side, the ventilation of O_2 is essentially controlled by the ocean circulation and mixing processes. Broadly, ventilation refers to the exchange of waters between the surface layer and the ocean interior (Talley et al., 2011), and involves a wide range of physical processes such as the wind-driven shallow overturning associated with the Subtropical cells (Brandt et al., 2015; Duteil et al., 2014; Eddebbar et al., 2019), the formation of mode and intermediate waters (Claret

55   et al., 2018; Sallee et al., 2010, 2012; Gnanadesikan et al., 2012) and the lateral (isopycnal) eddy stirring (Rudnickas et al., 2019; Gnanadesikan et al., 2013, 2015). These circulation systems are ultimately driven by the atmospheric winds and air-sea buoyancy fluxes which exhibit significant interannual, decadal and multi-decadal variability.

Fluctuations in ventilation rates as well as ocean stratification are known to impact both the O_2 levels (Ridder & England, 2014; Duteil et al., 2014; McKinley et al., 2003) and the distribution of isopycnal potential vorticity (IPV), a dynamical

60   tracer which is proportional to the local stratification and the Coriolis parameter. The use of the absolute value of the Coriolis parameter in the formula, indicated by *, guarantees that the relationship with stratification holds with the same sign in both hemispheres, so that higher IPV* indicates stronger stratification and vice versa. A strong winter-time convective mixing will produce weakly stratified, O_2-rich water masses (low IPV* and high O_2), and vice versa. These properties are then brought together into the ocean interior following the pathway of large-scale ocean currents.

65 In this study, we build upon this relationship, and we explore the overarching hypothesis that isopycnic potential vorticity (IPV*) may be used as a proxy for O_2 which may provide a path to predict the evolution of O_2, with a focus on the North Pacific basin. In the North Pacific, the Pacific Decadal Oscillation (PDO) is a leading mode of climate variability, exerting the greatest control on stratification and O_2 (Ito et al., 2019). Together with the El Niño Southern Oscillation (ENSO) at interannual timescales, it modulates the isopycnal surfaces in the tropics, and influences the depth of the winter mixed-layer

70 ventilation and the ventilation processes at mid-latitudes. Our specific objectives are to analyze Earth System Models (ESMs) to evaluate the hypotheses that (1) the ocean ventilation (IPV*) regulates O_2 variability in the oceans, (2) the ventilation-O_2 linkage provides the basis for the predictability of O_2 whenever IPV* is predictable, and (3) the linkage can be exploited to identify hotspots of O_2 changes in variability, means and extremes (see Methods).

Rather than working directly with the observational data, this study applies data-mining tools to a combination of Earth

75 System Model (ESM) outputs. ESMs provide a mathematical representation of underlying physical and biogeochemical processes in the form of coupled partial differential equations that are discretized and computationally integrated using high performance computing infrastructures. The time-evolving, three-dimensional distribution of physical and biogeochemical variables are generated as outputs of such calculations. Here we analyze outputs from the Coupled Model Intercomparison Project Phase 6 (CMIP6, Eyring, 2016), a major international effort with the primary objective of providing a standardized

80 framework for simulating the past, present, and future climate conditions. The participating modeling groups run their climate models under specified radiative forcing scenarios, and generate a comprehensive set of output datasets freely available to the scientific community through data portals and archives provided by the Earth System Grid Federation (ESGF). Using a suite of ESMs we will address the following questions:

- How robust is the relationship between O_2 and IPV* in the North Pacific across several ESMs and how may it
85 evolve by the end of the 21st century?

- What are the linkages between O_2 and IPV* versus large-scale modes of climate variability such as PDO and ENSO?

- Where are the hotspots of changes in IPV* and O_2, both in the historical period and in the projections, and are they co-located or differ in space and time?

90 To address the above questions, we apply a data-mining tool for dimensionality reduction and network analysis (δ-MAPS, Fountalis et al., 2018), and apply concepts such as information entropy (IE), and the standard Euclidean distance index (SED, Diffenbaugh and Giorgi, 2012). Since the above approaches are relatively new to the ocean biogeochemistry community, a brief overview is provided here, followed by detailed definitions in section 2.

First, δ-MAPS (Fountalis et al., 2018) combines feature extraction and network analysis into a single framework. The goal of δ-MAPS is to identify key features and to visualize how those features relate to one another. It establishes sets of spatially connected chunks of grid points sharing similar dynamical features, called domains. This is simpler and easier to interpret than empirical orthogonal functions (EOFs) which suffer from orthogonality constraints. It also allows to investigate the network of domains, but this step is skipped in this work. The benefits of δ-MAPS include simplicity, interpretability and overfitting prevention relative to conventional EOF-based approaches when extracting climate patterns from high-dimensional datasets.

Second, Information Entropy (IE) is a concept that measures the amount of randomness and therefore unpredictability in a dataset. Imagine a climate time series. IE measures how much information is contained in the data. If the time series is a random sequence, the entropy is high because there is more complexity or randomness. On the other hand, if it approximately follows a simple cosine curve, it is more predictable and simpler, thus IE is low.

Finally, the Standard Euclidean Distance (SED) index is a simple and flexible method used to detect *total* changes in one or more variables in a given dataset (in other words to identify regions that stand out for changes in means, extremes and variability), through measuring the distance in multi-variate space between a baseline period and any other (Diffenbaugh et al., 2008; Diffenbaugh and Giorgi, 2012, Williams et al., 2007). The SED is a non-parametric method, meaning it does not assume a specific probability distribution for the data. This flexibility makes it applicable to a wide range of datasets, regardless of their underlying distribution.

2 Materials and methods

In this section, we describe in more details the three tools recently developed for climate science applications and adopted in our analysis and how we calculate IPV*. The predictability potential of the fields examined is evaluated using the Information Entropy (IE). IE is defined following Prado et al. (2020) and is based on the recurrence of microstates for a recurrence plot (RP). A RP (Eckmann et al 1987) is a visualization technique for trajectory recurrence of a given dynamical system described in phase space by a matrix R_{ij} such that

$$R_{ij}(\epsilon) = \Theta\left(\epsilon - \left|x_i - x_j\right|\right), \; x_i \in \mathbb{R}, \; i,j = 1,2,\ldots,K, \tag{1}$$

where Θ is the heaviside function, $|\;\;|$ is an Euclidean distance, in our work, x_i and x_j are dynamical states at time steps i and j, ε is a threshold distance (the maximum distance between two states to be considered mutually recurrent), and K is the total number of time steps. R_{ij} is a matrix of "zeros" and "ones" which represent non-recurrent and recurrent states in phase space respectively, and it is explicitly dependent on ε. Corso et al. (2018) introduced the *Recurrence Entropy* quantifier, for which for a given time series, the probability of occurrence of microstates in its RP is quantified, without the need for a space-state

reconstruction. A microstate of size N is a NxN matrix inside RP, with probability of occurrence $P_k = n_k/N_{tot}$, where n_k are

125 the number of occurrences of the microstate in RP, and N_{tot} is the total number of possible configurations of 0 and 1 of the microstate (see Ikuyajolu et al (2021) and Prado et al 2020 for a detailed description). The information entropy IE is then defined as

$$IE(N_{tot}) = - \sum_{k=1}^{N_{tot}} P_k \ln P_k \qquad (2)$$

where k is the kth microstate. When IE is normalized by N_{tot} the case of IE=0 corresponds to perfect predictability, while

130 IE=1 represents full chaos. Furthermore, the explicit dependence of the entropy quantifier on ε is removed using the maximum entropy formulation. Prado et al. (2020) have shown that a value for which IE is maximum exists, does not vary much for varying ε and is strongly correlated with the Lyapunov coefficient of the system. We refer to Ikuyajolu et al (2021) for the details of the heuristic used to estimate the maximum entropy. In our work, we compute the entropy field of the deseasonalized and detrended IPV* (full signal) using 4 microstates.

135 δ-MAPS (Fountalis et al., 2018) is an unsupervised network analysis method that allows to identify spatially contiguous and possibly overlapping regions referred to as domains, and the lagged functional relationships between them. In short, domains are spatially contiguous regions that share a highly correlated temporal activity between grid cells of the same domain. In this work we apply it to the sea surface temperature (SST) anomaly field (see Data) to identify the major modes of climate variability in the north Pacific in a reanalysis and in the ESMs. δ-MAPS is an alternative approach to reduce the

140 dimensionality of spatio-temporal data to EOFs (standard or rotated). The orthogonality between EOF components complicates the interpretation of the results, especially when comparing models and observational datasets, as discussed, for example, in Dommenget and Latif (2002) and Falasca et al. (2019), and δ-MAPS offers a powerful solution to this problem. Given any spatio-temporal fields, its local homogeneity is hypothesized to be highest at "epicenters" or "cores". For each grid point, a local homogeneity is defined as the average pairwise cross-correlation between that grid cell and a set of K

145 nearest neighbors (see Fountalis et al., 2018 for details). Cores are then determined as neighbors of points where the local homogeneity is a local maximum and above a threshold δ. Each core is iteratively expanded and merged using a greedy algorithm to iteratively find domains as large as possible that are (i) spatially contiguous, (ii) include at least a core and (iii) have homogeneity higher than δ. δ is computed using a significance test for the unlagged cross-correlations. Given any random pair of grid points, the significance of the Pearson's correlation of their timeseries is assessed through the Bartlett's

150 formula (Box et al., 2011) with the null hypothesis of no coupling. The significance of each correlation is tested for a user-specified significance level α, and δ is computed as the average of significant correlations. Here, we applied δ-MAPS with K = 8 and α = 0.01.

The identification of hotspots of change follows the approach introduced by Diffenbaugh and Giorgi (2012) (which builds on Williams et al., 2007 and Diffenbaugh et al., 2008 and references therein), and applied by Turco et al. (2015) to the analysis

155 of global atmospheric data. Hotspots are quantified through a Standard Euclidean Distance index (SED) that aggregates the changes in means, variability and extremes of the given spatio-temporal field according to:

$$SED = \sqrt{\sum_{i=1}^{Nind} \sum_{j=1}^{4} \left(\frac{ind_{ij}}{p95(|ind_{ij}|)} \right)^2} \qquad (3)$$

We compute two SED indices, separately for O_2 and IPV*. N_{ind} is the total number of indicators per each variable and i the index identifying each indicator, j spans the seasons, so that ind_{ij} is the ith indicator in the jth season, and p95 is the 95th

160 percentile. Here we consider December-January-February as (boreal) winter, March-April-May as spring, and so on. We consider three indicators for each variable, evaluating changes in means, variability and extremes between two periods of equal length. *Period 1* covers 1950-1981 (1958-1986 for reanalysis and E3SM-2G ocean hindcast), and *Period 2* 1983-2014 (1986-2014 for reanalysis and hindcast) for the historical time, and 2036-2067 and 2069-2100 for the projected future. In equation (3) indicators of both periods are normalized on the 95th percentile calculated over *Period 1*, in order to fairly

165 compare changes of hotspots intensity over time. We chose not to compare 2069-2100 with 1950-1981, but with 2036-2067 instead, because we want to track changes in each period compared to the preceding timeslot in order to quantify how rapidly they occur in future projections compared to historical. We compute the indicators point by point using the Climate Data Operator (Schulzweida, 2022) as follows:

- Changes in means are estimated in each season separately by $Ind1 = yseasm_2 - yseasm_1$, where *yseasm1* and

170 *yseasm2* are multi-year seasonal means in *Period 1* and *2*, respectively.

- Changes in multi-year seasonal variability are evaluated by (i) detrending each variable point by point in the two periods separately, (ii) computing the multi-year seasonal standard deviation of these detrended fields, yseasσ, for each period for each season, (iii) computing *ind2* as the percentual changes such that $Ind2 = 100 \cdot \left(\frac{yseas\sigma_2 - yseas\sigma_1}{yseas\sigma_1} \right)$.

- Finally, changes in extremes (in our case specifically overshots of IPV* and undershots of O_2) are computed through the

175 following steps: (i) for each season, we compute at each grid point the multi-year seasonal O_2 minimum or IPV* maximum over *Period 1* and we consider it as a threshold (one threshold map per season); (ii) we count how many times in each corresponding season of *Period 2* O_2 < threshold$_{O2}$ (IPV* > threshold$_{IPV*}$) is verified; (iii) the percentage of occurrences computed at point (ii) is taken as indicator of percentual changes in extremes and estimated by $Ind3 = 100 \cdot \left(\frac{N_{occ}}{N_T} \right)$, where N_{occ} is the number of extremes occurrences (by season) and N_T is the total number of months in all

180 the corresponding seasons (96 for the models and 87 for reanalysis and hindcast).

We obtain three groups of four indicators (one per season) for each variable that are then used to compute the SED indices. Finally, the IPV* (m^{-1} s^{-1}) is used as a proxy of stratification and is defined as the isopycnic potential vorticity (Talley et al., 2011) with the absolute value of the Coriolis parameter in its formula:

185

$$IPV* = \frac{|f|}{g} N^2 \qquad (4).$$

Here N^2 is the Brunt–Väisälä frequency, g is the gravity acceleration and f is the Coriolis parameter. IPV is a conservative tracer in frictionless and adiabatic circulation. IPV* is calculated over the three-dimensional ocean volume using Eq. 5 and in this work we consider the 0-200 m vertical weighted average. This procedure allows us to compare datasets with different

190 vertical discretization.

3 Data

We consider four ESMs from the CMIP6 catalog, a hindcast and reanalysis data as summarized in Table 1. whenever multiple ensemble members were available, we selected the first (r1i1p1f1). All ESMs are forced by the historical radiative

195 forcing from 1850 to 2014. For the ESMs we analyze the monthly model output from 1950 to 2014. We further discuss future scp585 scenarios and focus on the 2036-2100 period, indicated as *future*.

The hindcast is a new ocean-ice biogeochemistry simulation (referred to as the G-Case), E3SMv2.0-BGC (hereafter, E3SM-2G, Takano et al, in prep), based on the Model for Prediction Across Scales-Ocean (MPAS-O), an ocean component of the Energy Exascale Earth System Model (E3SM) version 2 (Golaz et al., 2022). Details on ocean physics updates can be found

200 in Golaz et al. (2022). One of the major updates is the introduction of Redi isopycnal mixing (Redi, 1982) in version 2. Along with ocean physics updates, we also incorporated a uniform background vertical diffusion specifically for ocean biogeochemistry simulations to enhance ocean carbon uptake and thermocline ventilation of dissolved inorganic carbon (DIC). Incorporation of these ocean mixing (parameterizations) results in improved representation of climatological O_2 distributions in the version2 from its predecessor (Burrows et al., 2020). The Marine Biogeochemistry Library (MARBL,

205 Long et al, 2021) is used to simulate the ecosystem dynamics and cycling of biogeochemical elements. After the model spin-up, the model is forced by a meteorological reanalysis dataset, JRA-55do version 1.4 (Tsujino et al., 2020) from 1958 onward. Given its availability, we consider the 1958-2014 interval for the E3SM-2G hindcast and the ORAS4 reanalysis. All the data are remapped at 1°x1° horizontal resolution.

210

Table 1. CMIP6 Earth System Models, global ocean hindcast and reanalysis used in this work.

Modeling Group/Center	Model Name	Atmospheric Component/Resolution	Oceanic Component/ Resolution	Reference
National Oceanic and Atmospheric Administration, Geophysical Fluid Dynamics Laboratory	GFDL-ESM4	AM4.0, ~1°, 49 levels	OM4 MOM6, 0.5°x0.5°, 75 vertical levels (hybrid pressure/isopycnal)	(Dunne et al., 2020)
Canadian Earth System Model version 5	CanESM5	CanAM5, T63 (~2.8º), 49 levels	CanNEMO, 45 vertical levels, NEMO3.4.1, ORCA1 tripolar grid, 1° with refinement to 1/3° within 20° of the equator	(Swart et al., 2019)
NorESM Climate modeling Consortium	NorESM2-LM	CAM-OSLO, 2° resolution; 32 levels.	MICOM, 1°, 70 vertical levels	(Seland et al.,2020)
Institut Pierre-Simon Laplace	IPSL-CM6A-LR	LMDZ, NPv6, N96; 1.25°Lat x 2.5° Lon, 79 levels	NEMO-OPA (eORCA1.3, tripolar primarily 1°, 75 vertical levels.	(Boucher et al., 2020)
Department of Energy, Energy Exascale Earth System Model	E3SMv2.0-BGC (E3SM-2G)	JRA55do reanalysis (55km, 3hr resolution)	MPAS-O (30 to 60km resolution)	(Golaz et al, 2022; Takano et al., in prep)
ECMWF Ocean reanalysis System	ORAS4	_	Global, 1°, 42 Levels	(Balmaseda et al.,2012; Mogensen et al.,2012)

We begin our analysis with a brief evaluation of the ESM biases in the two main fields of interest, IPV* and O_2. For the

IPV*, the ocean reanalysis dataset is used for validating the model outputs. For O_2, we can only contrast the annual mean O_2

215   climatology between the World Ocean Atlas (Garcia et al., 2019) and the ESMs (Fig. 1).
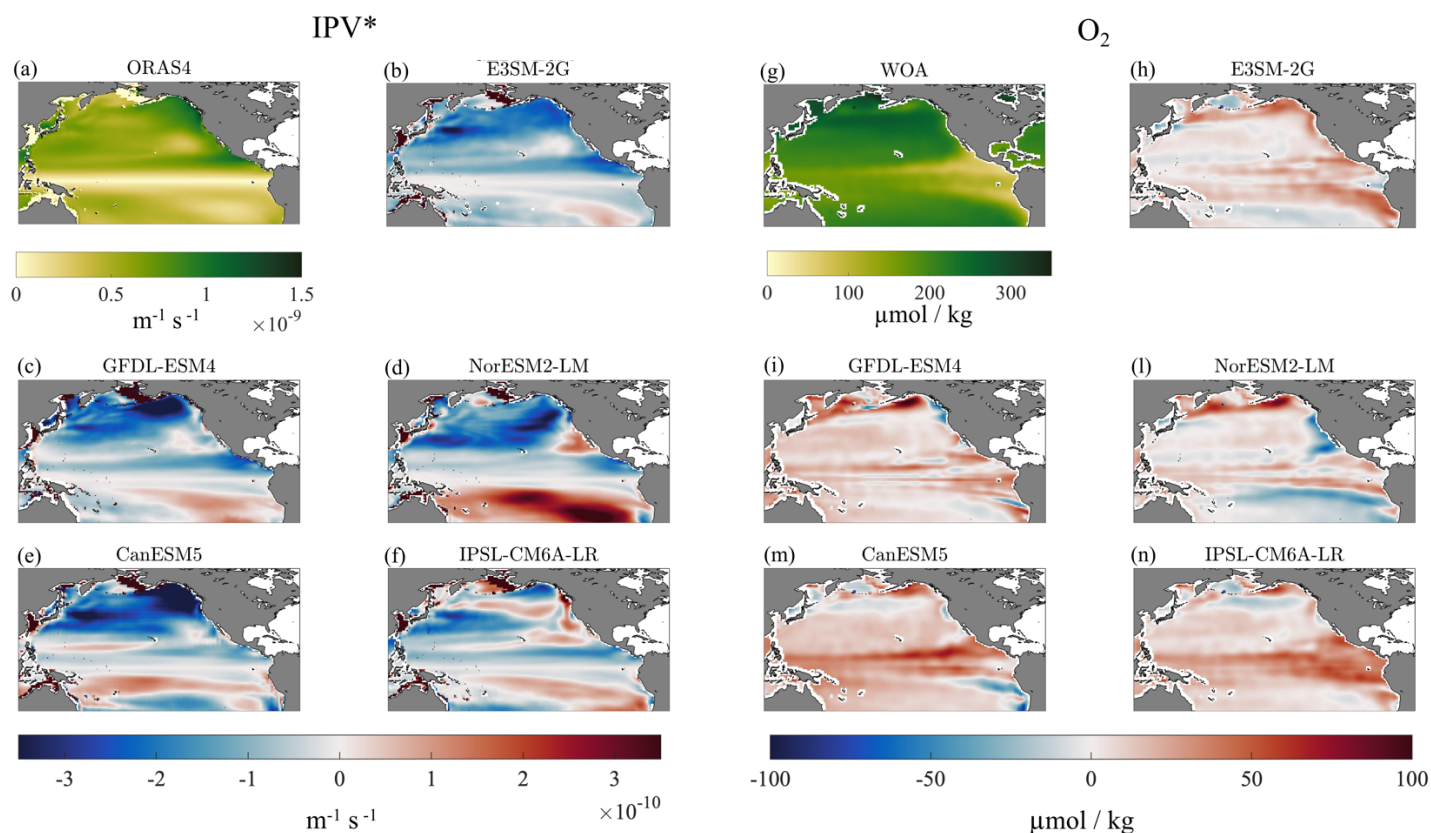
Figure 1. (Left) IPV* annual mean climatology (1959-2014) weighted averaged over 0-200 m depth in the North Pacific basin. (a)
ORAS4. (b-f) Model biases (model – ORAS4) difference. (Right) O_2 annual mean climatology (1950-2014) weighted averaged over 0-200
m depth. (g) World Ocean Atlas climatology. (h-n) Model biases (model – WOA) difference.

220   The E3SM-2G hindcast is forced by the observed atmospheric state and not surprisingly displays the lowest model bias and

root mean square error (RMSE). The RMSE of the modelled IPV* are 5.1 10^{-9} m^{-1} s^{-1} (E3SM-2G), 4.9 10^{-9} m^{-1} s^{-1} (GFDL-

ESM4), 5.4 10^{-9} m^{-1} s^{-1} (CanESM5), 4.9 10^{-9} m^{-1} s^{-1} (NorESM2-LM) and 5.5 10^{-9} m^{-1} s^{-1} (IPSL-CM6A-LR), while for O2 are,

respectively, 15.8 micro mol/kg (E3SM-2G), 19.4 micro mol/kg (GFDL-ESM4), 23.7 micro mol/kg (CanESM5), 18.8 micro

mol/kg (NorESM2-LM), 22.2.6 micro mol/kg (IPSL-CM6A-LR). Overall, the IPV* and O_2 biases have broadly

225   anticorrelated patterns, with the models being generally less stratified and more oxygen rich than observed in the extra-

tropical North Pacific, and often too stratified and with a larger O_2 deficit than observed south of the Equator. However,

maximum and minimum biases in the two fields only seldom coincide. Regionally, the E3SM-2G is generally less stratified than observed with a relatively low O_2 bias and an overestimation of approximately 10 mmol/kg in the subtropical thermocline of the North Pacific basin. The hindcast performs especially well in the tropical thermocline. Among the CMIP6 models, CanESM5 shows a slightly higher IPV* underestimation in the subpolar gyre and a O_2 overestimation in the subtropics compared to the other ESMs, while NorESM2-LM emerges as the most stratified south of the Equator. In O_2 there is the tendency that larger biases (positive or negative) are found in the tropical thermocline and the tropical/subtropical boundaries. The sign and magnitude of the biases are model dependent. Interestingly, models generally overestimate O_2 at the subpolar latitudes.

4 Results

4.1 Predictability potential

We begin our analysis with a discussion of the predictability potential of IPV*, quantified through the information entropy (IE, see Methods). The goal is to verify if and where IPV* has an elevated predictability skill, owing to the presence of quasi-recurrent behaviors in its time-series. We also aim to examine whether O_2 is correlated with IPV* in regions where the latter has a high predictability potential. As a reminder, IE values close to 1 indicate high complexity and unpredictability, and close to 0 perfect predictability (the signal is recurrent, for example constant or periodic). IE maps for IPV* are shown in Fig. 2 for both historical and future times, with superposed the contours of the areas where the (lagged) anticorrelation between IPV* and O_2 is at least -0.5 (see Suppl. Fig. S1 for the anticorrelation and lag maps). Higher predictability in the historical period is found in the area most impacted by ENSO. The predictability potential is generally highest along two stripes enclosing the ENSO pattern and excluding the upwelling cold tongue regions. The distribution of IE follows broadly that found in a much longer simulation of the IPSL model covering the past 6,000 years and analyzed by Falasca et al. (2022). The western boundary current region and the Kuroshio-Oyashio extensions have low predictability across all datasets considered. In NorESM2-LM and CanESM5, and to a lesser degree in ORAS4 and IPSL-CM6A-LR, the higher predictability of the ENSO area extends to the north-eastern portion of the basin. In general, in both the hindcast and the models, strong anticorrelations between the time series of IPV* and O_2 (<-0.5) coincide with low IE regions and are linked to ENSO affecting concurrently stratification and O_2 in the tropics and south of the upwelling area. Very limited IPV* predictability is found in the central and western North Pacific, where the variability is dominated by the PDO signal which does not emerge as easily predictable both in the interval considered, in agreement with e.g. Gordon et al. (2021) and, at least in the IPSL model, across the second half of the Holocene (Falasca et al., 2022). In those areas, anticorrelations between O_2 and IPV* are also relatively weak (generally > -0.4 but for NorESM2-LM). The entropy and the regions where the evolution of IPV* and O_2 are strongly anticorrelated do not change significantly in the future projections in the four models.
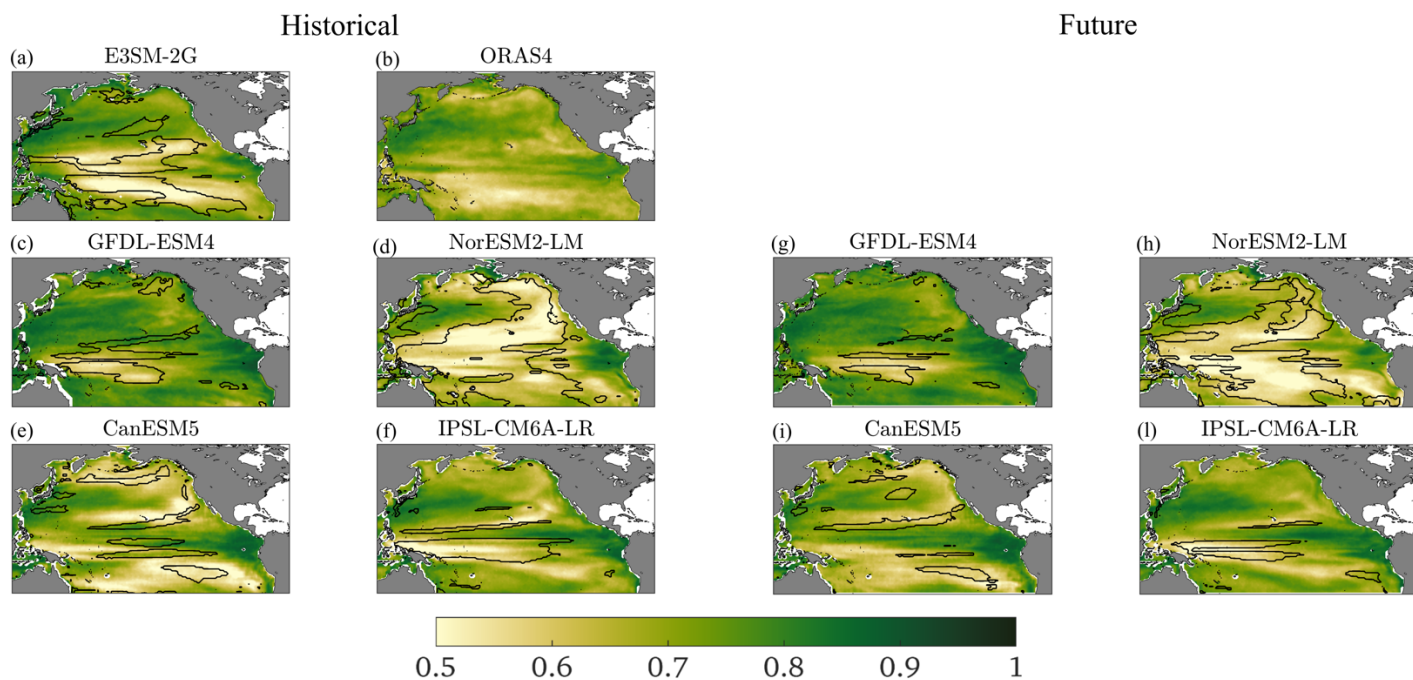
Figure 2: IPV* entropy field in the historical interval (left) and in the future (right) for the ESMs, and in the historical 1958-2014 period for the hindcast and ORAS4 with superposed the contours of the areas where IPV* and O_2 time series are anticorrelated with correlation coefficients < -0.5.

4.2 Trends and PDO impact

The limited predictability found in the North Pacific does not exclude the possibility of the PDO modulating both IPV* and O_2 inventories simultaneously. We therefore quantify the (linear) impact of the PDO on the two fields of interest, and then evaluate the evolution of their residuals. If the PDO is the main predictor of IPV* and O_2 distributions, its impact on the two fields should be strongly anticorrelated and larger than the residual. As mentioned in the Introduction, the objective is to verify if the greater availability of IPV* observations, reanalyses and modeled fields could be used to extrapolate information about O_2 and its evolution in time, bypassing the need to run full biogeochemical models or measure O_2 directly. We use δ-MAPS (see Material and Methods) applied to the SST field to evaluate the main modes of Pacific climate variability, ENSO and PDO with a greater focus on the latter, and their time evolution in the models, the ocean hindcast and the reanalysis. While the evolution of ENSO using δ-MAPS is straightforwardly described by the timeseries of the cumulative anomalies in the ENSO-related domain (e.g. Falasca et al., 2019), for the PDO we must consider the difference

between the SST cumulative anomalies of two domains. The domains are identified by the complex network algorithm, and we applied a 5-yr running mean to produce the PDO time-series shown in Fig. 3. The domains shape and size are indicated

275   in Fig. 4.

For ORAS4 and E3SM-2G, we computed the 0-lag correlations between these timeseries and the commonly defined indices of PDO (following Mantua et al. 1997) and Nino34 (average SST anomalies over the box 5ºN-5ºS, 170ºW-120ºW) for validation. Both timeseries are retrieved from NOAA (https://psl.noaa.gov/data/climateindices/list/). Correlation coefficients are 0.92 for PDO and 0.93 for ENSO in ORAS4, and are 0.53 for PDO and 0.88 for ENSO in E3SM-2G.

280   Moving to the models (Fig. 3), in the historical period GFDL-ESM4 slightly underestimates the PDO strength, while the opposite is verified in CanESM5 and NorESM2-LM. In the latter, the frequency of the signal, which changes in sign every 10-15 years, is also higher than observed. By the end of the 21st century, the strength of the PDO remains unaltered in GFDL-ESM4 and IPSL-CM6A, while decreases in NorESM2-LM and especially in CanESM5, following a decrease in size of the eastern domain. A decrease in amplitude and increase in frequency of the PDO was found also in several models in the

285   CMIP5 ensemble (Li et al., 2020).
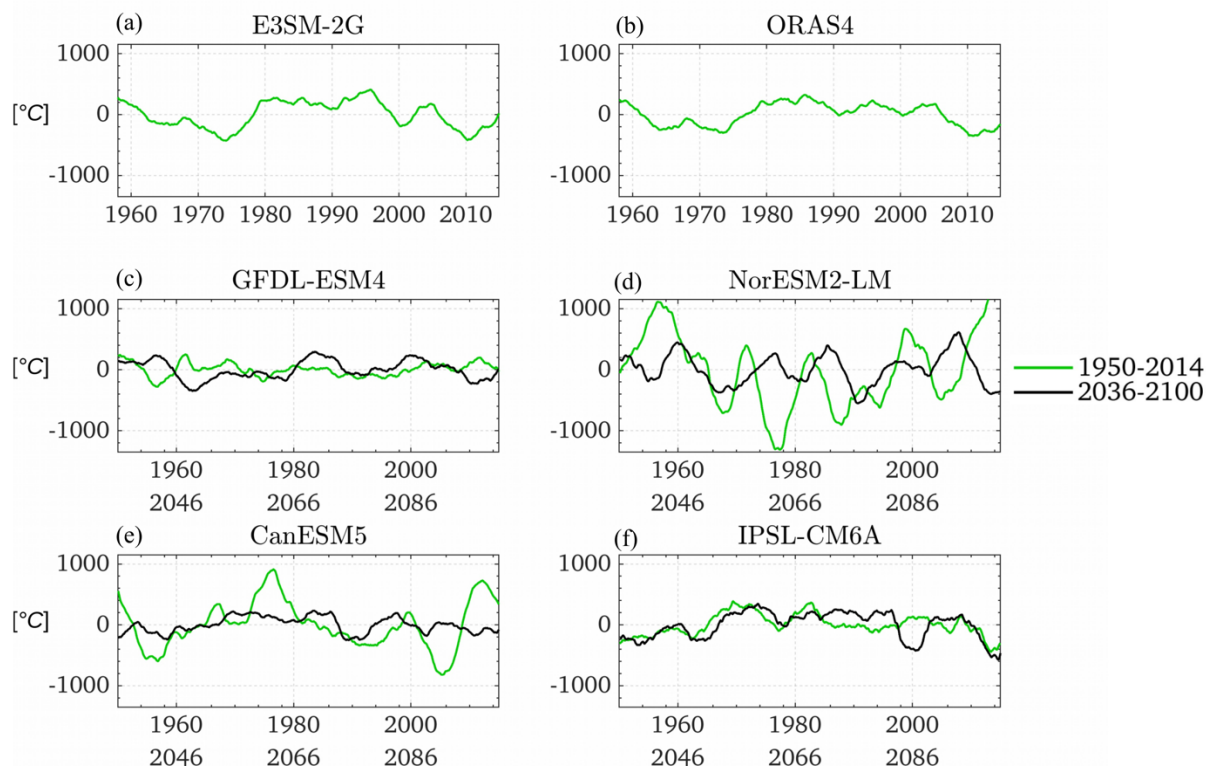
Figure 3: PDO indices (SST cumulative anomalies) calculated using δ-MAPS (see text) in the historical and future time periods.

With the indices, PDO(t), we can separate the residual component of the fields of interest that is not linearly forced by the PDO in all datasets as a function of time following, for example, Kucharski et al. (2008) and defining for O_2 (but the same procedure was applied to IPV*):

$$O_{2res}(x,y,t)=O_2(x,y,t)-O_{2PDO}(x,y,t) \qquad (5),$$

where

$$O_{2PDO}(x,y,t) = b_{O2}(x,y)*PDO(t) \qquad (6)$$

and $b_{O2}(x,y)$ is constant in time and determined by least-square fitting through a linear regression for each dataset. Figure 4 shows b_{IPV*} and b_{O2} for all datasets with superposed the boundaries of the domains corresponding to the ENSO and those contributing to the PDO in the historical period. In most cases there is an overall anticorrelation signal between the maps for the two fields, as to be expected, but also several important differences. First, the regions where b_{O2} is strongest (both positive and negative values) do not correspond to minima and maxima in b_{IPV*}. Second, the equatorial upwelling tends to have a strong positive signal in b_{O2} and only a weak one, but of the same sign, in b_{IPV*}. Third, the PDO impacts on the two fields considered vary substantially among models, as quantified by the correlation among the respective fields indicated in the figure, with GFDL being the closest to the hindcast and, for the IPV* case, also to the reanalysis. In NorESM the anticorrelation between the regression fields is too strong and the PDO has both a shape and loading in the Pacific interior which is different than observed. CanESM5 and IPSL display domain-averaged positive correlations, with important biases at the equator and along the eastern boundary with respect to the hindcast. The correlations between the $b_{O2}(x,y)$ and $b_{IPV*}(x,y)$ maps are indicated in the figure. Furthermore, the trends of the residuals have comparable amplitude of the PDO-forced signal in both fields in the historical period in all cases (see Suppl. Fig. S2). We will further discuss the trends shape when presenting *Ind1*.
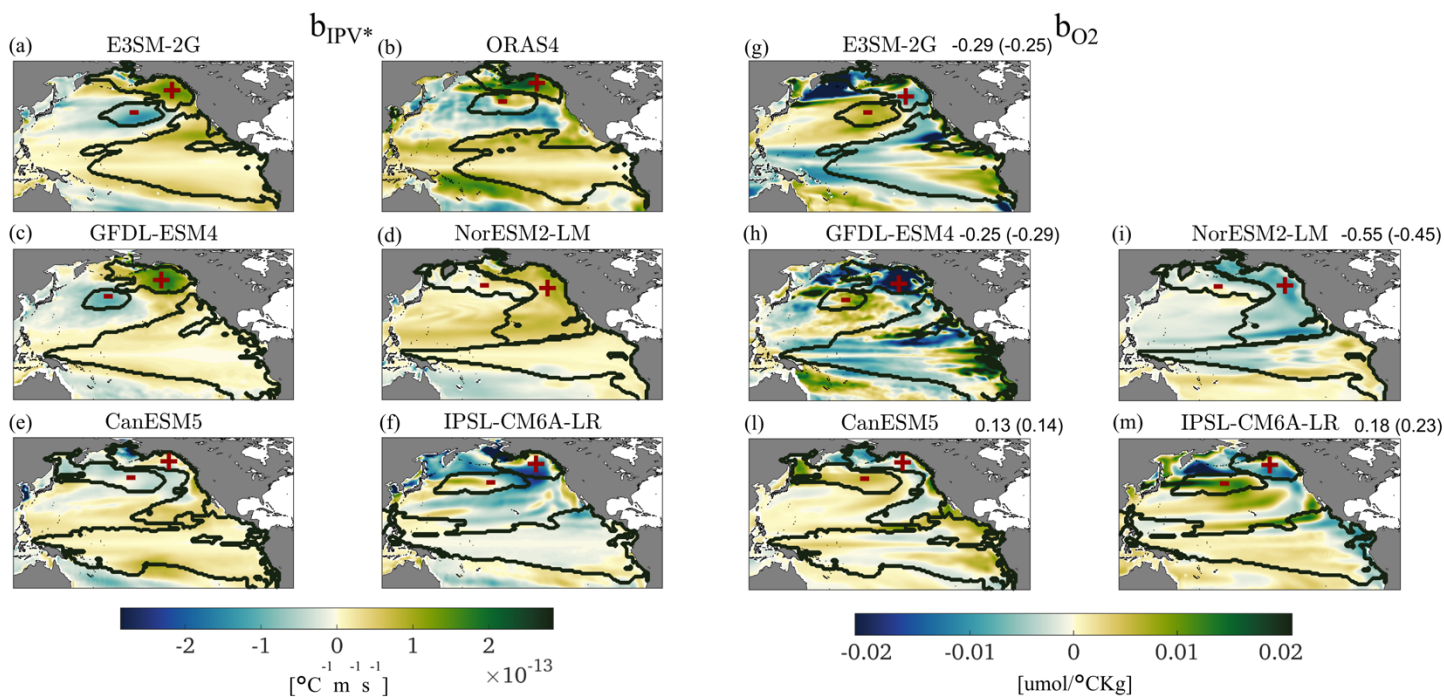
Figure 4: b_{IPV*} (left) and b_{O2} (right) regression coefficient maps with superposed contours of the ENSO and of the PDO+ and PDO-domains. The correlation coefficients among the corresponding maps for the same model or hindcast are also indicated. Color limits are fixed as +/- 3 standard deviations of the ensemble for each variable over the whole area (+/- 2.85 10 for IPV* and +/- 0.021 for O_2). Values in parentheses are c.c. computed north of 20°N. All the c.c. values passed the shuffling significance test at 5% level (see Suppl. Mat.)
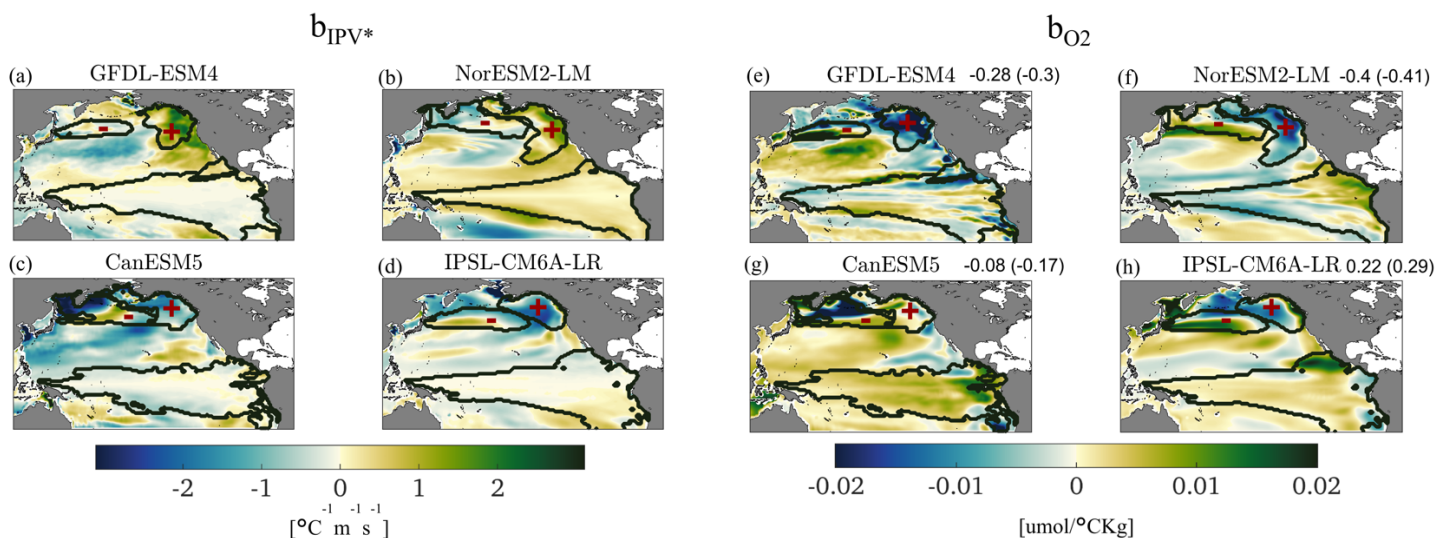
Figure 5: as in Figure 4 but for the future projections. Color limits are fixed as +/- 3 standard deviations of the ensemble for each variable

over the whole area (+/- 3.01 10^{-13} for IPV* and +/- 0.02 for O_2). Values in parentheses are c.c. computed north of 20°N. All the correlation coefficients passed the significance test at 5% level (see Suppl. Mat.)

Moving to the projections, the regression coefficient maps do not significantly change in three models considered (Fig. 5). In CanESM5, on the other hand, b_{IPV*} changes sign over most of the domain. The residual trends, when compared to the
320 regression coefficients, are stronger and dominate the evolution of both fields, especially in the subtropical and subpolar gyres of the North Pacific (Suppl. Fig. S3), superseding the PDO signal.

4.3 Hot spots of change

As a last step, we evaluate changes in means, extremes and variability in the residual of both variables using the indicators introduced in the Methods. For the historical time, we divide the 1950-2014 interval in two periods of equal length covering
325 1950-1981 and 1983-2014 (1958-1986 and 1986-2014 for E3SM-2G). We evaluated the indicators using all seasons averaged together or separately, and found that differences across seasons were small, as measured by the standard deviation of the indicators (Suppl. Fig. S4-S6). In the following we discuss only the all-seasons averaged indicators without any loss of information.
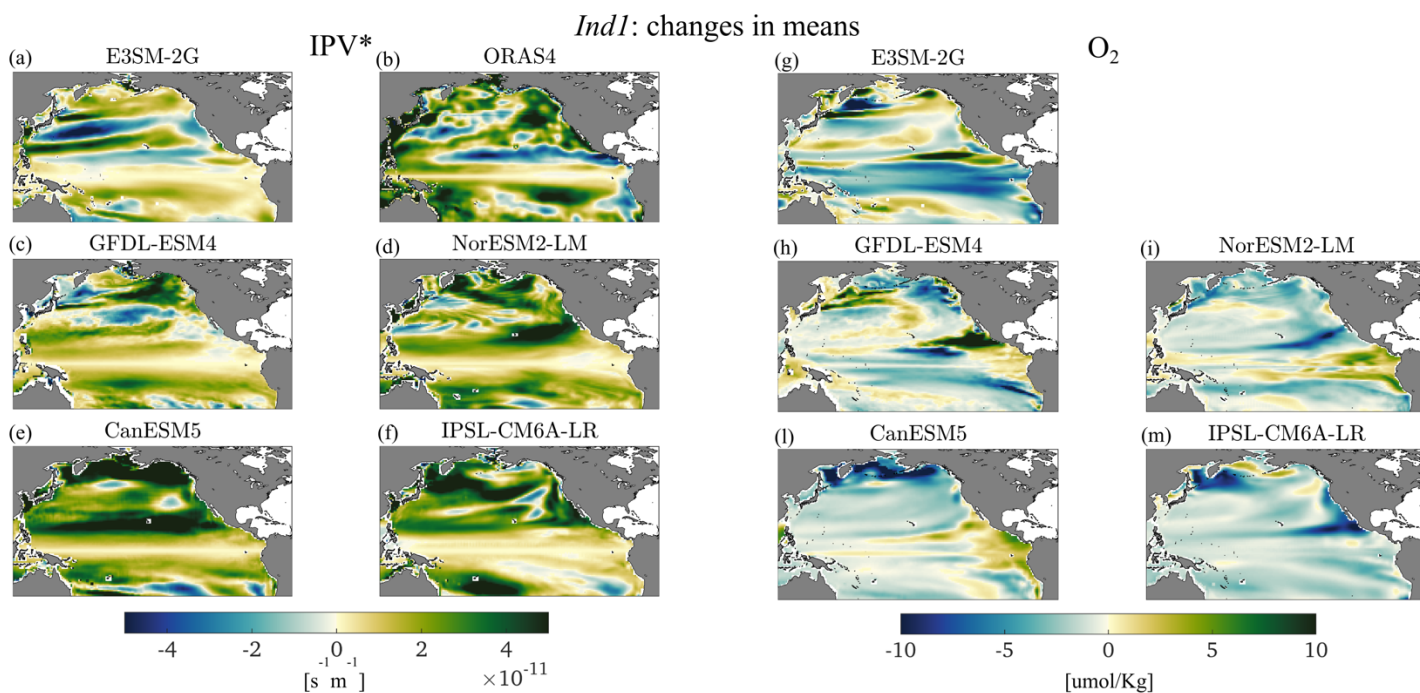
330 **Figure 6.** 1950-2014 *Ind1* for residual IPV* (left) and residual O_2 (right). All indicator maps are obtained by averaging the respective four seasonal maps.

Ind1 in Fig. 6 shows the changes in the residual mean fields, which have very similar patterns to the linear trend in both
IPV*$_{res}$ and O$_{2res}$ (see Suppl. Fig. S2). By 2015 stratification has increased nearly everywhere in the ESMs, but for the

335 equatorial upwelling region where is mostly unchanged, and the Kuroshio-Oyashio extension. In ORA4 there is also a
prominent band where stratification decreases between 10° and 20°N extending from the coast of the American continent to
150°W in the second period and in the overall trend. O$_{2res}$ decreases in most of the north Pacific but for the upwelling areas
along the coast of Peru', Central America, and the California Current System in all simulations but for IPSL-CM6A-LR, the
North Equatorial Current region in the E3SM-2G hindcast, GFDL-ESM4 and CanESM5, the Equatorial upwelling band in

340 NorEMS-LM, and portions of the subpolar gyre around Alaska in E3SM-2G and IPSL-CM6A-LR. The O$_{2res}$ *Ind1* maps
suggest that a significant decrease in O$_2$ should have affected the subpolar gyre around the Kamchatka peninsula.
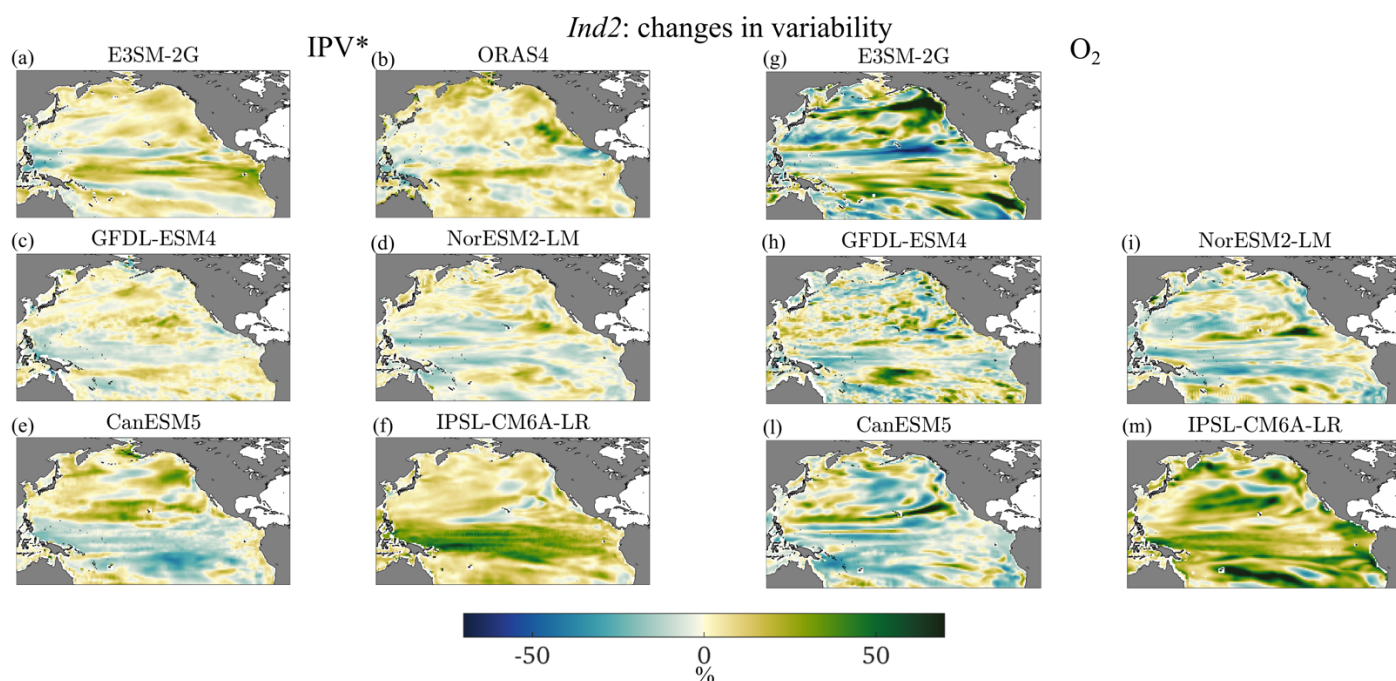
Figure 7. 1950-2014 *Ind2* for residual IPV* (left) and residual O$_2$ (right).

345 Indicators of change in (seasonal) variability (*Ind2,* Fig. 7) show strong differences across models in patterns and, at least for
O$_2$, intensity. Whenever corresponding maps of O$_2$ and stratification have the same sign and comparable amplitude at
corresponding locations, they indicate that increments or decreases in IPV* variability at seasonal scales are associated with
corresponding increments in 0-200m O$_{2res}$ variability. In the hindcast, changes are greater for residual O$_2$ than stratification.
This is verified also in three of the models in the north-eastern extratropics. Among the models, GFDL-ESM4 and NorESM-

350   LM show patchy changes, both positive and negative, across the domain, with the smallest amplitudes among the datasets

considered. CanEMS5 undergoes predominately positive changes north of the equator in IPV*$_{res}$ and negative to the south of

it, while the variability in the O$_{2res}$ field decreases also in the central portion of the subtropical gyre. In IPSL-CM6A-LM the

variability increases nearly everywhere in both fields, but especially at the equator and to the south of it in IPV*$_{res}$ and more

uniformly at all latitudes in O$_{2res}$.

355
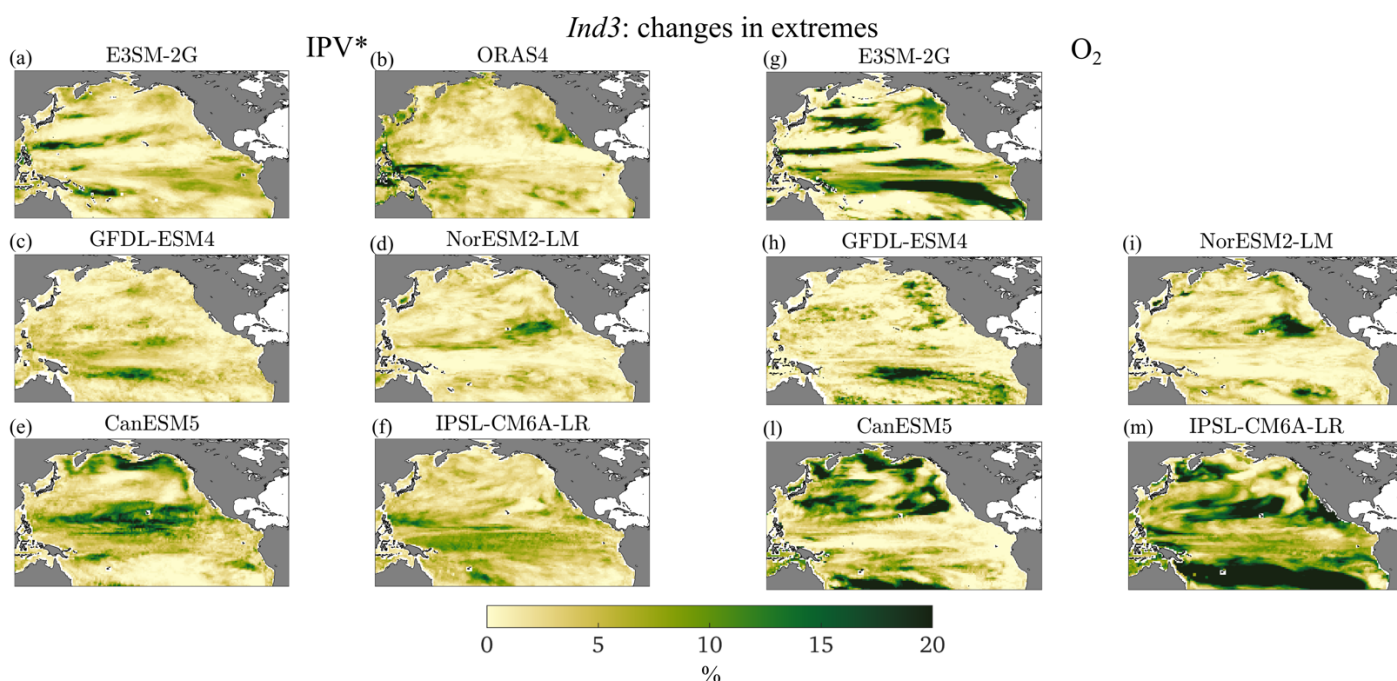
Figure 8. 1950-2014 *Ind3* for residual IPV* (left) and residual O$_2$ (right).

Changes in extremes (*Ind3*) for the residual O$_2$ field are stronger than for stratification (Figure 8). Episodes of strong O$_2$

decrease and stratification increase are more frequent in *Period 2*. For O$_{2res}$ the equatorial regions to the north and south of

360   the upwelling band emerge as especially impacted in the E3SM-2G hindcast and GFDL-ESM4, while the subtropical gyre

displays an increase in extreme events nearly everywhere (CanESM5 and IPSL-CM6A-LM), or at its boundary (E3SM-2G)

or in its eastern portion (GFDL-ESM4 and NorEMS2-LM). The subpolar gyre is affected especially in CanESM5 and IPSL-

CM6A-LM. Changes in IPV*$_{res}$ extremes have less clear latitudinal differences and do not display a robust (across models)

intensification at extratropical latitudes. In ORAS4 maxima are found near the California Current System and in the Warm

365   Pool area.

	E3SM-2G	GFDL-ESM4	NorESM2-LM	CanESM5	IPSL-CM6A-LR
Ind1	**-0.06** (0.01)	**-0.12 (-0.14)**	**-0.23 (-0.16)**	**-0.31 (-0.24)**	**-0.12 (-0.08)**
Ind2	**0.26 (0.22)**	**0.26 (0.17)**	**0.3 (0.32)**	**0.3 (0.19)**	**0.2 (0.22)**
Ind3	**0.1 (-0.1)**	**0.29** (0.03)	**0.52 (0.63)**	**0.11 (0.43)**	-0.02 **(0.21)**

Table 2 1950-2014 Correlation coefficients (c.c) between the corresponding indicator maps for IPV* and O_2. Bold underlined values that passed the shuffling significance test at 5% level (see Suppl Mat.). Numbers in parentheses reflect c.c. computed north of 20°N.

370   Table 2 summarizes the correlation coefficients between the maps of the three indicators for the two fields considered. Coefficients are negative for all models but small for *Ind1*, slightly larger in amplitude and positive for the variability indicator in all cases, and very small for *Ind3* in the hindcast, CanEMS5 and IPSL-CM6A-LM, while larger in amplitude and positive for GFDL-ESM4 and especially NorESM-LM.

The resulting hotspot indices (SED), computed separately for the IPV*$_{res}$ and the O_{2res} indicators (see Methods) are reported

375   in Fig. 9. Except for IPSL-CM6A-LM, the hotspots are found outside the equatorial band. Those for O_2 are generally stronger along the eastern part of the subtropical gyres, in the eastern part of PDO region and along the California upwelling system, and the IPV*$_{res}$ hotspots are more commonly found over the western parts of the basin and along the southern boundary of the subtropical gyre. This result suggests a longitudinal decoupling between hotspots in O_2 and stratification in at least three of the models and in the hindcast, with NorESM2-LM being the exception due to the simulated superposition of

380   the changes in extremes in the two fields.
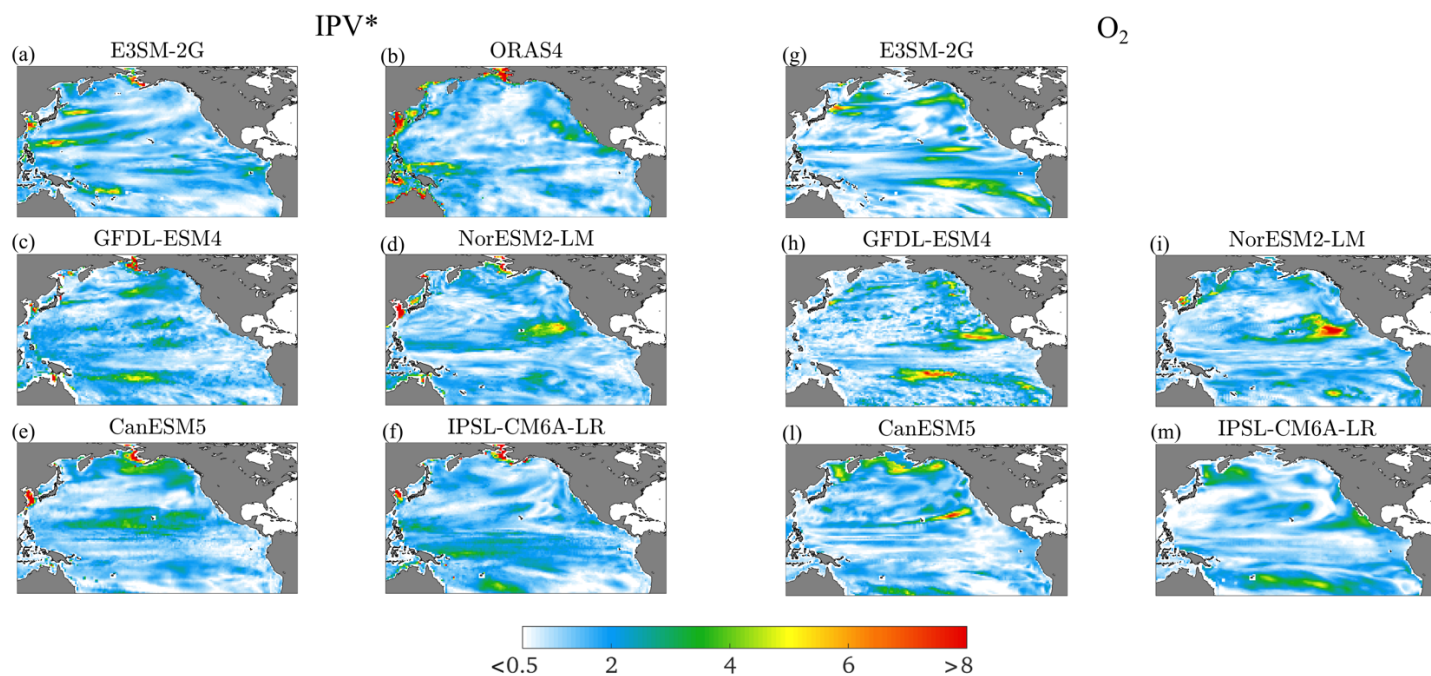
Figure 9. 1950-2014 SED *index* for IPV*$_{res}$ (left) and residual O$_{2res}$ (right). The colorscale is realized with rgbmap (Greene, 2023).

The maps of the indicators for the future projections follow in Fig. 10-12, again averaged over seasons for consistency with

385   the historical ones. The associated standard deviations are reported in Suppl. Fig. S8-S10. In the projections, the seasonal

differences are slightly stronger compared to the historical period for *Ind1* (IPV*$_{res}$) and *Ind3* (both IPV*$_{res}$ and O$_{2res}$),

especially for CanESM5, NorESM2-LM and IPSL-CM6A-LR, in the northern subpolar gyres for *Ind1* IPV*$_{res}$ (Suppl. Fig.

S8) and along the subtropical and the northern subpolar gyres for *Ind3* IPV*$_{res}$ (Suppl. Fig. S10). Standard deviations for

Ind3 O$_{2res}$ are stronger along the extratropical gyres and weaker in the tropical upwelling region (Suppl. Fig. S10). Areas of

390   higher standard deviations in the projections are, however, associated with much stronger values of *Ind1* and *Ind3* compared

to the historical period. In the projections, *Ind1,* which for a perfectly linear trend would represent the trend itself,

strengthens significantly and is stronger than the actual trend shown in Supp. Fig. S3, indicating an acceleration of the

changes in the last portion of the 21st century. This is especially relevant for IPV*$_{res}$ north of the Equator. Stratification

increases everywhere but for areas in the southern hemisphere which have different extension in the four models and are

395   found in the central and eastern portions of the basin. O$_{2res}$ decreases everywhere but for small areas around the equatorial

upwelling band. The decrease is very strong along the northern boundary of the Pacific Ocean and, depending on the model,

at the subtropical gyre boundary (NorESM-LM and to a lesser degree CanESM5) and south of the Equator along the coast of Central and South America (IPSL-CM6A-LR).
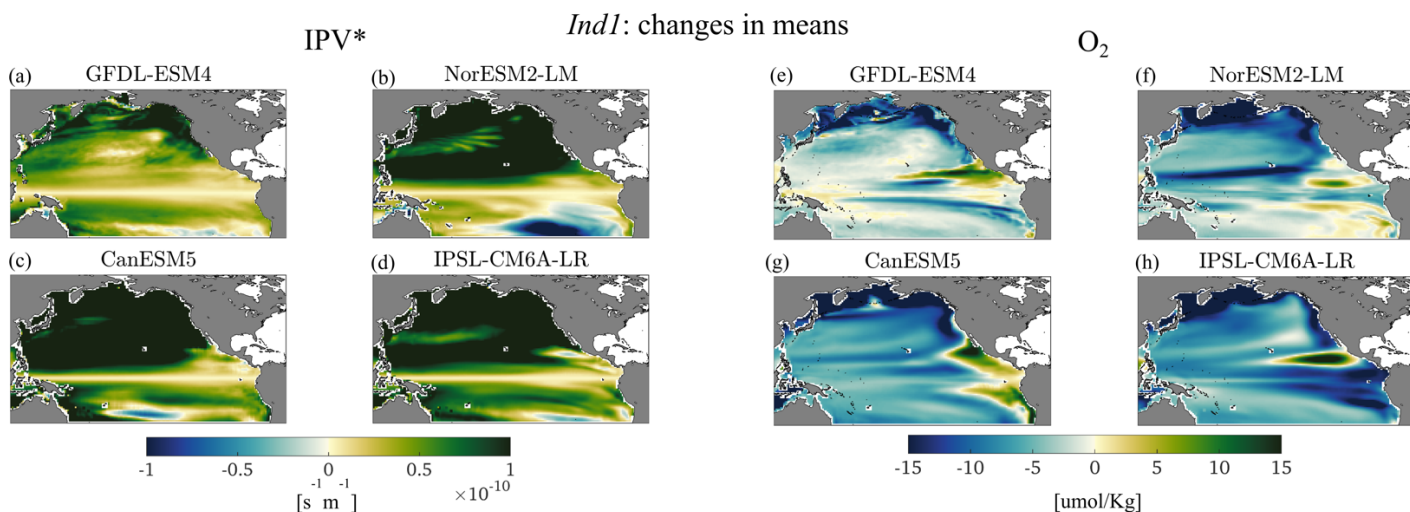
Figure 10. 2036-2100 *Ind1* for IPV*$_{res}$ (left) and O$_{2res}$ (right).
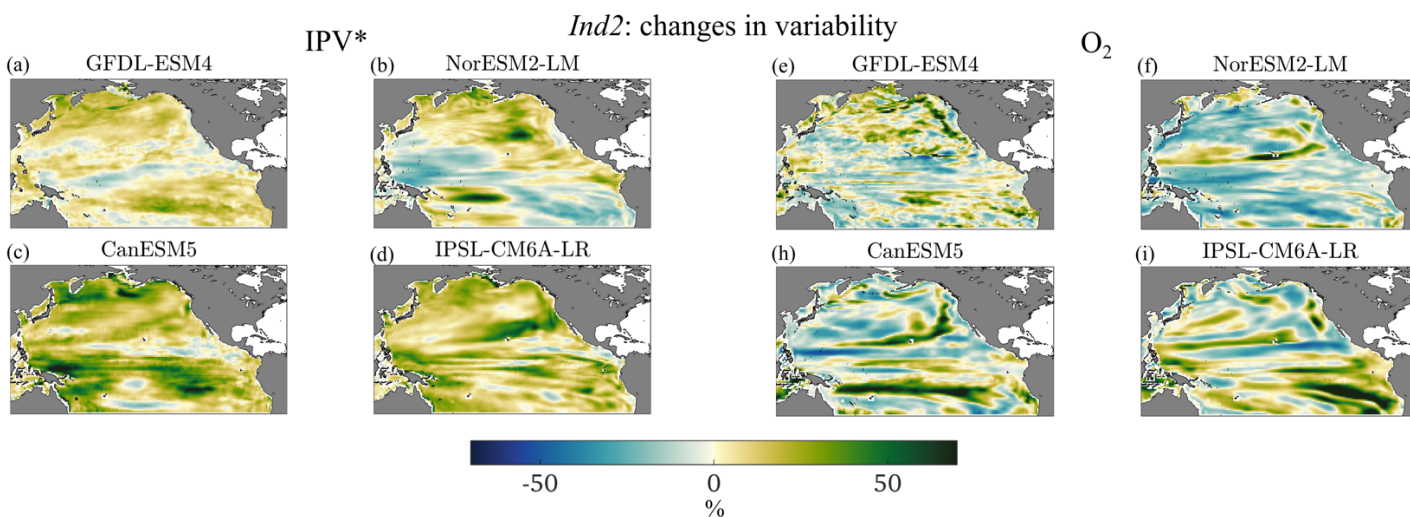
Figure 11. 2036-2100 *Ind2* for IPV*$_{res}$ (left) and O$_{2res}$ (right).

In terms of variability, very few areas with comparable sign and amplitude (which would indicate comparable increases or decreases) can be seen in Fig. 11 when comparing the two variables. IPV*$_{res}$ variability increases almost everywhere in three

of the models, NorESM2-LM being the exception in the Warm Pool and to the south of the Equator in the eastern portion of the basin. O_{2res} variability increases in patchy areas mostly in the eastern half of the basin in GFDL-ESM4, only along the southern boundary of the subtropical gyre in NorESM2-LM, roughly along the boundaries of the gyres in CanESM5 and along the northern gyre boundary and south of the Equator in IPSL-CM6A-LR. Lastly, extremes (*Ind3*, Fig. 12) are found to

410   increase nearly everywhere but for the equatorial upwelling area in both variables for CanESM5 and IPSL-CM6A-LR, in the northern hemisphere in NorESM2-LM, in the ENSO region, especially in the Warm Pool, and in GFDL-ESM4 along the northern boundary of the basin for IPV*$_{res}$ and along the northern and southern portion of the considered domain for O_{2res}. Correlations among maps of the two variables are generally very small for all indicators in the projections (Table 3) with $|c.c.| < 0.4$, except for *Ind1* in NorESM2-LM and CanESM5.

415
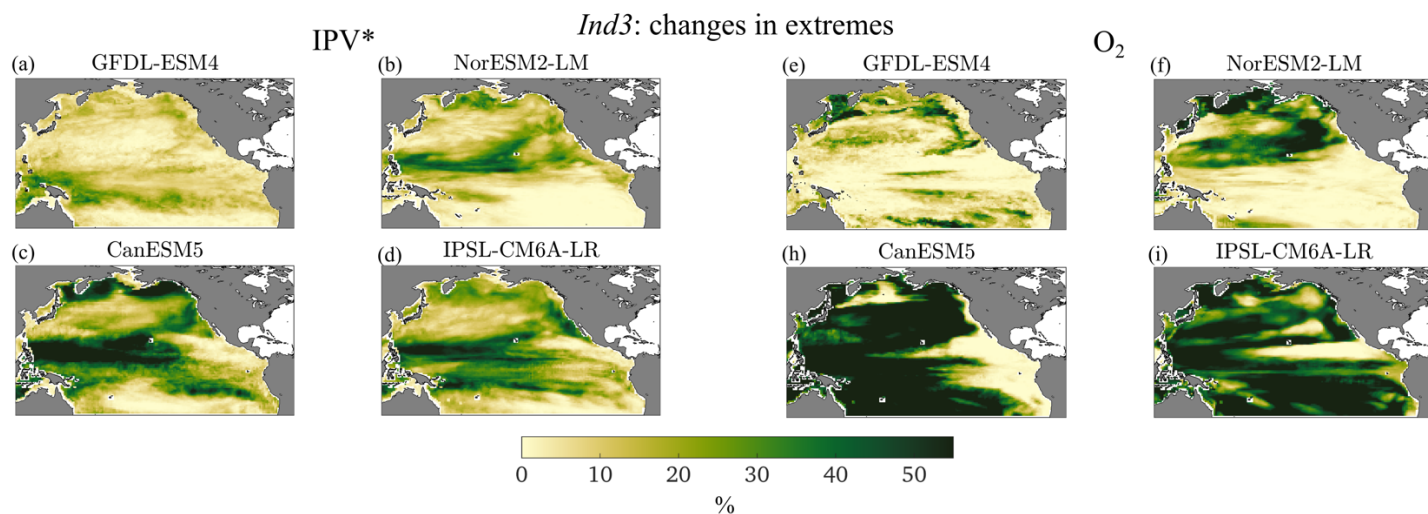
Figure 12. 2036-2100 *Ind3* for IPV*$_{res}$ (left) and residual O_{2res} (right). The percentage shown reaches 60% (three times more than during historical, Figure 8).

	GFDL-ESM4	NorESM2-LM	CanESM5	IPSL-CM6A-LR
Ind1	**- 0.25 (-0.18)**	**-0.54 (-0.22)**	**-0.61 (-0.59)**	**-0.32 (-0.28)**
Ind2	**0.34 (0.32)**	**0.12 (0.21)**	**0.18 (0.19)**	0.04 (**0.06**)
Ind3	**-0.05 (0.51)**	**0.39 (0.4)**	**0.2** (0.01)	**0.11** (0.04)

Table 3. 2036-2100 Correlation coefficients (c.c) between the corresponding indicator maps for IPV* and O_2. Bold underlined values that passed the shuffling significance test at 5% level (see Suppl. Mat.). Numbers in parentheses reflects c.c. computed north of 20°N.
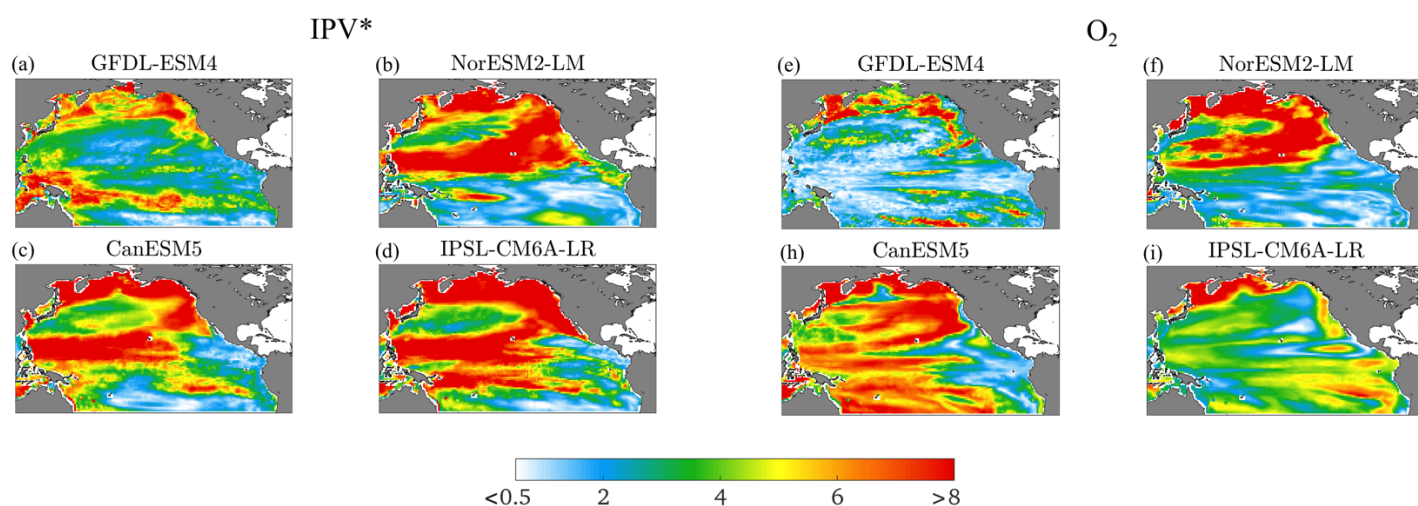
Figure 13. 2036-2100 SED *index* for IPV*$_{res}$ (left) and O_{2res} (right). The colorscale is produced with rgbmap (Greene, 2023).

5. Conclusions

Earth System Models (ESMs) have made significant progress in simulating the Earth's climate and biogeochemical processes and have provided valuable insights into what the future may hold. However, there are still challenges and limitations in accurately capturing ocean biogeochemical dynamics. Improving model performance requires continued collaboration between biogeochemists, climate modelers, and observationalists. The availability of observational data for biogeochemical processes is often limited, especially in remote and poorly sampled regions (e.g., subsurface waters or far away from population centers). This lack of data makes it difficult to validate and constrain model simulations accurately. Linkages between physical climate and ocean O_2 can be exploited to better understand and to improve predictive skills of

biogeochemical tracers. We anticipate an increase in autonomous observations of biogeochemical variables such as BGC-ARGO floats soon, which will provide better data coverage for O_2 concentrations from seasonal to interannual timescales,

435   improving the chances to identify new relationships between ocean O_2 and physical variables such as temperature and salinity. The analysis approaches and the findings from this study will help focusing the upcoming observational analysis and modeling efforts. The overarching hypothesis of this study was that the spatial-temporal variability of O_2 reflects that of ocean ventilation, which can be measured by the magnitude of the isopycnic potential vorticity (IPV). There has been a wide range of mechanisms suggested for the connection between O_2 and upper ocean ventilation, many of which can be

440   represented in the ESMs. In this study IPV* is chosen as the tracer of physical ventilation processes, where a strong ventilation is assumed to generate a negative anomaly in IPV*, which then is advected and mixed through the transport processes. The same strong ventilation is expected to inject O_2-rich surface waters into the interior ocean, leading to a negative correlation between O_2 and IPV*. This simplistic view has been challenged through the analyses of data complexity, linkages to the dominant climate modes, and patterns of extreme events. First, the robustness of the relationship

445   between O_2 and IPV* was examined for the present and future climate. The entropy analysis identified the areas where IPV has a high predictability potential (generally along two stripes enclosing the ENSO pattern and excluding the upwelling cold tongue regions), which are also areas where O_2 and IPV show a strong anti-correlation. This behavior is robust across all the analyzed datasets and does not change significantly in the future projections in the four ESMs. This relationship provides a linkage between IPV* (easily retrievable from physical variables) and O_2, and IPV* can be a good proxy for O_2 showing a

450   strong predictability in the areas where the anticorrelation (lagged or simultaneous) is strong and IE is lower than in the rest of the basin. The greater availability of temperature and salinity (and therefore stratification) observations from ARGO floats, reanalyses and modeled fields could be used in conjunction to the fewer co-located observations of O_2 to validate our findings and further extrapolate information about O_2 and its evolution in time in these tropical areas.

Secondly, the variability of O_2 and IPV* was examined in relation to large-scale modes of climate variability in the North

455   Pacific. In general, ENSO-dominated regions are characterized by a higher predictability potential for IPV*, in the tropics and south of the upwelling regions including the northeastern portion of the basin, where O_2 is negatively correlated with it. On the other hand, PDO-dominated regions show very little IPV* predictability. The low predictability extends to the western boundary current region and the Kuroshio-Oyashio extensions. In addition, in the extra-tropical North Pacific, where the PDO has its center of action, the imprint of PDO on O_2 and IPV*, and the trends of their residuals have comparable

460   amplitude in the historical period. This is not verified in the future projections, when the trends become increasingly dominant. Correlations in the PDO regression maps are generally quite small across models.

Thirdly, the hotspots of IPV* and O_2 variability were examined in the historical period and in the future projections. Overall, the historical hotspot indices or SED, computed separately for IPV* and O_2, suggest a longitudinal decoupling of changes for all datasets considered but NorESM2-LM. Most of hotspots of change are in the extratropics. The geographic distribution of

465   IPV* and O_2 SED can differ from each other. O_2 SED are generally stronger in the eastern parts and along the California upwelling system, while IPV* strongest hotspots are mostly found over the western parts of the basin and southern boundary

of the subtropical gyre. The intensity of the SED increases over time, and much stronger and more widely distributed hotspots are found in the projections. In the projections, the northern part of the North Pacific is characterized by a strong SED index for both O_2 and IPV* in all the models. For three out of four models, strong IPV* SED indices are located along

470   the northern subtropical gyre, where also the O_2 SED are high. IPSL-CM6A-LR is an exception, and the SED indices for the two fields remain strongly de-coupled. Larger changes and hotspots are found at the gyre boundaries and in the northern portion of the basin, from the Kamchatka peninsula to the Gulf of Alaska. There is a general agreement that the loss of O_2 is linked to the strong increase in stratification, but there are significant differences in the regions affected across models, pointing to the area of further investigation.

475   Biogeochemical processes involve intricate interactions between multiple components of the earth system. These processes are often nonlinear and can be influenced by feedback loops, making their representation and coupling with physical variables (such as IPV*) complex and challenging to interpret, therefore requiring advances in diagnosis methods and interpretation. To accurately assess model performance, continued efforts to develop metrics for model evaluation and intercomparison are needed. In this study we presented a set of tools that may contribute to this end. These quantitative

480   approaches together with advances in observation-based gridded products, can better characterize and extract information about linkages between physical and biogeochemical variables. In particular, the availability of biogeochemical data, including dissolved oxygen, while still sparse compared to that of physical data, has grown significantly in the last decade. Using the ARGO-O_2 dataset as a primary input, Giglio et al. (2018) and Sharp et al. (2022) generated time-evolving maps of dissolved O_2 concentrations from seasonal to interannual timescales using machine learning tools. The ever-increasing data

485   volume and the generation of (multiple) gridded data products will enable new types of quantitative analysis and this works provides a framework for it and for new models-observations intercomparisons.

Data availability

The python version of δ-MAPS is available at https://github.com/FabriFalasca/py-dMaps . The code for the Information Entropy computation is available at https://github.com/FabriFalasca/NonLinear_TimeSeries_Analysis . Climate indices used

490   in this study are from NOAA at https://psl.noaa.gov/data/climateindices/list/). The CMIP6, Earth system model output used in this study is available via the Earth System Grid Federation (https://esgf-node.llnl.gov/search/cmip6/).

Authors contribution

LN performed all analysis, AB and TI conceived the study, TI and YT helped supervise the project, YT led the E3SM-2G development and integration. AB took the lead in writing the manuscript. All authors provided critical feedback and helped

495   shape the research, analysis and manuscript.

Competing interests

The authors declare that they have no conflict of interest.

Acknowledgements

500 We thank Fabrizio Falasca and Ilias Fountalis, who developed several of the software tools for the data mining component of this project. The authors were supported by the Department of Energy, Regional and Global Model Analysis (RGMA) Program, Grant No. 0000253789.

505

References

Balmaseda, M. A., Mogensen, K. and Weaver, A. T.: Evaluation of the ECMWF ocean reanalysis system ORAS4. Q.J.R. Meteorol. Soc., doi: 10.1002/qj.2063, 2012.

Box, G. E., Jenkins, G. M. and Reinsel, G. C.: Time series analysis: forecasting and control, Wiley, 2011.

510 Boucher, O., Servonnat, J., Albright, A. L., Aumont, O., Balkanski, Y., Bastrikov, V., Bekki, S., Bonnet, R., Bony, S., Bopp, L., Braconnot, P., Brockmann, P., Cadule, P., Caubel, A., Cheruy, F., Codron, F., Cozic, A., Cugnet, D., D'Andrea, F., Davini, P., Lavergne, C. de, Denvil, S., Deshayes, J., Devilliers, M., Ducharne, A., Dufresne, J.-L., Dupont, E., Éthé, C., Fairhead, L., Falletti, L., Flavoni, S., Foujols, M.-A., Gardoll, S., Gastineau, G., Ghattas, J., Grandpeix, J.-Y., Guenet, B., Guez, L., Guilyardi, É., Guimberteau, M., Hauglustaine, D., Hourdin, F., Idelkadi, A., Joussaume, S., Kageyama, M.,

515 Khodri, M., Krinner, G., Lebas, N., Levavasseur, G., Lévy, C., Li, L., Lott, F., Lurton, T., Luyssaert, S., Madec, G., Madeleine, J.-B., Maignan, F., Marchand, M., Marti, O., Mellul, L., Meurdesoif, Y., Mignot, J., Musat, I., Ottlé, C., Peylin, P., Planton, Y., Polcher, J., Rio, C., Rochetin, N., Rousset, C., Sepulchre, P., Sima, A., Swingedouw, D., Thiéblemont, R., Traore, A. K., Vancoppenolle, M., Vial, J., Vialard, J., Viovy, N., and Vuichard, N.: Presentation and evaluation of the IPSL-CM6A-LR climate model, J. Adv. Model. Earth Sy., 12, e2019MS002010, https://doi.org/10.1029/2019MS002010,

520 2020.

Brandt, P., Bange, H. W., Banyte, D., Dengler, M., Didwischus, S.-H., Fischer, T., Greatbatch, R. J., Hahn, J., Kanzow, T., Karstensen, J., Körtzinger, A., Krahmann, G., Schmidtko, S., Stramma, L., Tanhua, T., and Visbeck, M.: On the role of circulation and mixing in the ventilation of oxygen minimum zones with a focus on the eastern tropical North Atlantic, Biogeosciences, 12, 489–512, https://doi.org/10.5194/bg-12-489-2015, 2015.

525 Burrows, S. M., Maltrud, M., Yang, X., Zhu, Q., Jeffery, N., Shi, X., Ricciuto, D., Wang, S., Bisht,G., Tang, J., Wolfe, J., Harrop, B. E., Singh, B., Brent,L., Baldwin, S., Zhou,T., Cameron-Smith, P., Keen, N., Collier, N., Xu, M., Hunke, E. C., Elliott, S. M., Turner, A. K., Li, H., Wang, H., Golaz, J.-C., Bond-Lamberty, B., Hoffman, F. M., Riley, W. J., Thornton, P. E., Calvin,K., Leung, L. R.: The DOE E3SM v1.1 biogeochemistry configuration: Description and simulated ecosystem-climate responses to historical changes in forcing. Journal of Advances in Modeling Earth Systems, 12(9), e2019MS001766.

530 https://doi.org/10.1029/2019ms001766 , 2020.

Claret, M., Galbraith, E.D., Palter, J.B., Bianchi, D., Fennel, K., Gilbert, D. and Dunne, P.J.: Rapid coastal deoxygenation due to ocean circulation shift in the northwest Atlantic. Nature Clim Change 8, 868–872, https://doi.org/10.1038/s41558-018-0263-1, 2018.

Corso, G., Prado, T., Lima, G., Kurths, J., and Lopes, S.: Quantifying entropy using recurrence matrix microstates. Chaos

535 28:083108. doi: 10.1063/1.5042026 , 2018.

Deutsch C., Ferrel A., Seibel B., Pörtner H.O., Huey R.B.: Ecophysiology. Climate change tightens a metabolic constraint on marine habitats. Science, 348(6239):1132-5. doi: 10.1126/science.aaa1605. PMID: 26045435. 2015.

Diffenbaugh, N. S., and Giorgi, F.: Climate change hotspots in the CMIP5 global climate model ensemble, Clim. Change, 114 (3–4), 813–822, 2012.

540 Diffenbaugh, N.S., Giorgi, F. and Pal, J.S.: Climate change hotspots in the United States. Geophys Res Lett 35, doi:10.1029/2008GL035075 , 2008.

Dommenget, D. and Latif, M.: A cautionary note on the interpretation of EOFs. Journal of Climate, 15, 216–225, 2002.

Dunne, J. P., Horowitz, L. W., Adcroft, A. J., Ginoux, P., Held, I. M., John, J. G., Krasting, J. P., Malyshev, S., Naik, V., Paulot, F., Shevliakova, E., Stock, C. A., Zadeh, N., Balaji, V., Blanton, C., Dunne, K. A., Dupuis, C., Durachta, J., Dussin,

545 R., Gauthier, P. P. G., Griffies, S. M., Guo, H., Hallberg, R. W., Harrison, M., He, J., Hurlin, W., McHugh, C., Menzel, R., Milly, P. C. D., Nikonov, S., Paynter, D. J., Ploshay, J., Radhakrishnan, A., Rand, K., Reichl, B. G., Robinson, T., Schwarzkopf, D. M., Sentman, L. T., Underwood, S., Vahlenkamp, H., Winton, M., Wittenberg, A. T., Wyman, B., Zeng, Y., and Zhao, M.: The GFDL Earth System Model version 4.1 (GFDL-ESM 4.1): Overall coupled model description and simulation characteristics, J. Adv. Model. Earth Sy., 12, e2019MS002015, https://doi.org/10.1029/2019MS002015, 2020.

550 Duteil, O., Böning, C.W., Oschlies, A.: Variability in subtropical-tropical cells drives oxygen levels in the tropical Pacific Ocean. Geophys Res Lett 41(24):8926–8934, 2014.

Eckmann, J. P., Kamphorst, S. O. and Ruelle, D.: Recurrence Plots of Dynmiacal Systems, Europhys. Lett. 4, 973 (1987).

Eddebbar, Y. A. et al.: El Niño-like physical and biogeochemical ocean response to tropical eruptions. J. Clim. 32, 2627–2649, 2019.

555 Eyring, V., Bony, S., Meehl, G. A., Senior, C. A., Stevens, B., Stouffer, R. J., and Taylor, K. E.: Overview of the Coupled Model Intercomparison Project Phase 6 (CMIP6) experimental design and organization, Geosci. Model Dev., 9, 1937–1958, https://doi.org/10.5194/gmd-9-1937-2016, 2016.

Falasca, F., Bracco, A., Nenes, A., and Fountalis, I.: Dimensionality Reduction and Network Inference for Climate Data

Using δ-MAPS: Application to the CESM Large Ensemble Sea Surface Temperature, J. Adv. Model. Earth Sy., 11, 1479–
560   1515, https://doi.org/10.1029/2019MS001654, 2019.

Falasca, F., Crétat, J., Braconnot, P. and Bracco: A. Spatiotemporal complexity and time-dependent networks in sea surface
temperature from mid- to late Holocene, Eur. Phys. J. Plus 135, 392, https://doi.org/10.1140/epjp/s13360-020-00403-x ,
2020.

Fountalis, I., Dovrolis, C., Bracco, A., Dilkina, B. and Keilholz, S.: δ-MAPS: from spatio-temporal data to a weighted and
565   lagged network between functional domains. Appl Netw Sci **3**, 21, https://doi.org/10.1007/s41109-018-0078-z , 2018.

Garcia, H. E., Boyer, T. P., Baranova, O. K., Locarnini, R. A., Mishonov, A. V., Grodsky, A., Paver, C.R, Weathers, K.W.,
Smolyar, I.V., Reagan, J.R., Seidov, D. and Zweng, M.M.: World ocean atlas 2018: Product documentation. A. Mishonov,
Technical Editor, 2019.

Giglio, D., Lyubchich, V. and Mazloff, M. R.: Estimating Oxygen in the Southern Ocean Using Argo Temperature and
570   Salinity. *J. Geophys Res. Oceans, 123* (6), 4280−4297. 2018.

Gilpin, W: Deep Reconstruction of Strange Attractors From Time Series. Cambridge, MA: Harvard University, 2020.

Gnanadesikan, A., Dunne, J. P., and John, J.: Understanding why the volume of suboxic waters does not increase over
centuries of global warming in an Earth System Model, Biogeosciences, 9, 1159–1172, https://doi.org/10.5194/bg-9-1159-
2012, 2012.

575   Gnanadesikan, A., Bianchi, D., and Pradal, M. A.: Critical role for mesoscale eddy diffusion in supplying oxygen to hypoxic
ocean waters, Geophys. Res. Lett., 40, 5194–5198, https://doi.org/10.1002/GRL.50998, 2013.

Gnanadesikan A., Pradal M., Abernathey R.: Isopycnal mixing by mesoscale eddies significantly impacts oceanic
anthropogenic carbon uptake. Geophys. Res. Lett. 42, 4249–4255. doi: 10.1002/2015GL064100, 2015.

Golaz, J.C., Van Roekel, L.P., Zheng, X., Roberts, A.F., Wolfe, J.D., Lin, W., Bradley, A.M., Tang, Q.; Maltrud, M.E.,
580   Forsyth, R.M. et al.: The DOE E3SM Model Version 2: Overview of the physical model and initial model evaluation. J.
Adv. Model. Earth Syst. 14, e2022MS003156, 2022.

Gordon, E. M., Barnes, E. A., and Hurrell, J. W.: Oceanic harbingers of Pacific Decadal Oscillation predictability in CESM2
detected by neural networks. Geophysical Research Letters, 48, e2021GL095392. https://doi.org/10.1029/2021GL095392,
2021.

585   Greene, C.: rgbmap color maps (https://www.mathworks.com/matlabcentral/fileexchange/46874-rgbmap-color-maps),
MATLAB Central File Exchange. Retrieved June 27, 2023

Ikuyajolu, O. J., Falasca, F. and Bracco, A.: Information Entropy as Quantifier of Potential Predictability in the Tropical
Indo-Pacific Basin. Front. Clim. 3:675840. doi: 10.3389/fclim.2021.675840, 2021.

Ito, T., Minobe, S., Long, M. C., and Deutsch, C.: Upper ocean O_2 trend.: 1958–2015, Geophys. Res. Lett., 44, 4214–
590   4223, https://doi.org/10.1002/2017GL073613, 2017.

Ito, T., Long, M. C., Deutsch, C., Minobe, S., and Sun, D.: Mechanisms of low-frequency oxygen variability in the North
Pacific. Global Biogeochemical Cycles, 33(2), 110–124. https://doi.org/10.1029/2018GB005987, 2019.

Kucharski, F., Bracco, A., Yoo, J.H. and Molteni, F.: Atlantic forced component of the Indian monsoon interannual variability. Geophys. Res. Lett. 35 (4) https://doi.org/10.1029/2007gl033037 , 2008.

595 Li, S., Wu, L., Yang, Y., Geng, T., Cai, W., Gan, B., Chen, Z., Jing, Z., Wang, G. and Ma, X.:The Pacific Decadal Oscillation less predictable under greenhouse warming. Nat. Clim. Chang. 10, 30–34, https://doi.org/10.1038/s41558-019-0663-x, 2020.

Long, M. C., Moore, J. K., Lindsay, K., Levy, M., Doney, S. C., Luo, J. Y., Krumhardt, K. M., Letscher, R. T., Grover, M., and Sylvester, Z. T.: Simulations With the Marine Biogeochemistry Library (MARBL), J. Adv. Model. Earth Sy., 13,

600 e2021MS002647, https://doi.org/10.1029/2021MS002647, 2021.

Marwan, N., Romano, M. C., Thiel, M., and Kurths, J.: Recurrence plots for the analysis of complex systems. Phys. Rep. 438, 237–329. doi: 10.1016/j.physrep.2006.11.001 , 2007.

Mantua, N. J., Hare, S. R., Zhang, Y, Wallace, J.M., Francis, R. C.: A Pacific interdecadal climate oscillation with impacts on salmon production Bull. Am. Meteorol. Soc., 78, pp. 1069-1080, 1997.

605 McKinley, G. A., Follows, M. J., and Marshall, J.: Mechanisms of air-sea CO2 flux variability in the equatorial Pacific and the North Atlantic. Global Biogeochemical Cycles, 18(2), C07S06. https://doi.org/10.1029/2003GB002179, 2004.

Mogensen, K., Alonso Balmaseda, M., Weaver, A.: The NEMOVAR ocean data assimilation system as implemented in the ECMWF ocean analysis for System4. ECMWF Technical Memorandum 668. 59 pages, 2012.

Nevison, C., Butler, J. H., and Elkins, J. W.: Global distribution of N2O and the ΔN2O-AOU yield in the subsurface ocean,

610 Global Biogeochem. Cy., 17, 1119, https://doi.org/10.1029/2003GB002068, 2003.

Prado, T., Corso, G., Santos Lima, G., Budzinski, R., Boaretto, B., Ferrari, F., Macau, E.E.N. and Lopes, S.R.: Maximum entropy principle in recurrence plot analysis on stochastic and chaotic systems. Chaos 30:043123. doi: 10.1063/1.5125921, 2020.

Redi, M.H.: Oceanic Isopycnal Mixing by Coordinate Rotation. Journal of Physical Oceanography, 12, 1154-1158, 1982.

615 Ridder, N. N. and England, M. H.: Sensitivity of ocean oxygenation to variations in tropical zonal wind stress magnitude, Global Biogeochem. Cy., 28, 909–926, 2014.

Rudnickas, D. Jr., Palter, J., Hebert, D., Rossby,H.T.: Isopycnal mixing in the North Atlantic oxygen minimum zone revealed by RAFOS floats J. Geophys. Res.: Oceans, 124, 10.1029/2019JC015148, 2019.

Sallée, J. B., Rintoul, S. R. and Wijffels, S. E.: Southern ocean thermocline ventilation. J. Phys. Oceanogr. 40, 509–529,

620 2010.

Sallée, J.B., Matear, R., Rintoul, S. et al.: Localized subduction of anthropogenic carbon dioxide in the Southern Hemisphere oceans. Nature Geosci 5, 579–584, https://doi.org/10.1038/ngeo1523, 2012.

Schulzweida, U.: CDO User Guide (2.1.0). Zenodo. https://doi.org/10.5281/zenodo.7112925, 2022.

Schmidtko, S., Stramma, L. And Visbeck, M.: Decline in global oceanic oxygen content during the past five decades. Nature

625 542, 335–339, https://doi.org/10.1038/nature21399 , 2017.

Seland, Ø., Bentsen, M., Olivié, D., Toniazzo, T., Gjermundsen, A., Graff, L. S., Debernard, J. B., Gupta, A. K., He, Y.-C.,

Kirkevåg, A., Schwinger, J., Tjiputra, J., Aas, K. S., Bethke, I., Fan, Y., Griesfeller, J., Grini, A., Guo, C., Ilicak, M., Karset, I. H. H., Landgren, O., Liakka, J., Moseid, K. O., Nummelin, A., Spensberger, C., Tang, H., Zhang, Z., Heinze, C., Iversen, T., and Schulz, M.: Overview of the Norwegian Earth System Model (NorESM2) and key climate response of CMIP6

630   DECK, historical, and scenario simulations, Geosci. Model Dev., 13, 6165–6200, https://doi.org/10.5194/gmd-13-6165-2020, 2020.

Sharp, J. D., Fassbender, A. J., Carter, B. R., Johnson, G. C., Schultz, C., and Dunne, J. P.: GOBAI-O$_2$: temporally and spatially resolved fields of ocean interior dissolved oxygen over nearly two decades, Earth Syst. Sci. Data Discuss. [preprint], https://doi.org/10.5194/essd-2022-308, in review, 2022.

635   Swart, N. C., Cole, J. N. S., Kharin, V. V., Lazare, M., Scinocca, J. F., Gillett, N. P., Anstey, J., Arora, V., Christian, J. R., Hanna, S., Jiao, Y., Lee, W. G., Majaess, F., Saenko, O. A., Seiler, C., Seinen, C., Shao, A., Sigmond, M., Solheim, L., von Salzen, K., Yang, D., and Winter, B.: The Canadian Earth System Model version 5 (CanESM5.0.3), Geosci. Model Dev., 12, 4823–4873, https://doi.org/10.5194/gmd-12-4823-2019, 2019.

Talley, L. D., Pickard, G. L., Emery, W. J. , Swift, J. H.: Descriptive Physical Oceanography: An Introduction, Academic
640   Press, London, 2011.

Turco, M., Palazzi, E., Hardenberg, J. and Provenzale, A.: Observed climate change hotspots Geophys. Res. Lett. **42** 3521–8, 2015.

Tsujino, H., Urakawa, L. S., Griffies, S. M., Danabasoglu, G., Adcroft, A. J., Amaral, A. E., Arsouze, T., Bentsen, M., Bernardello, R., Böning, C. W., Bozec, A., Chassignet, E. P., Danilov, S., Dussin, R., Exarchou, E., Fogli, P. G., Fox-
645   Kemper, B., Guo, C., Ilicak, M., Iovino, D., Kim, W. M., Koldunov, N., Lapin, V., Li, Y., Lin, P., Lindsay, K., Liu, H., Long, M. C., Komuro, Y., Marsland, S. J., Masina, S., Nummelin, A., Rieck, J. K., Ruprich-Robert, Y., Scheinert, M., Sicardi, V., Sidorenko, D., Suzuki, T., Tatebe, H., Wang, Q., Yeager, S. G., and Yu, Z.: Evaluation of global ocean–sea-ice model simulations based on the experimental protocols of the Ocean Model Intercomparison Project phase 2 (OMIP-2), Geosci. Model Dev., 13, 3643–3708, https://doi.org/10.5194/gmd-13-3643-2020, 2020.

650   Webber, C. L., Jr. and Zbilut, J. P.: Dynamical assessment of physiological systems and states using recurrence plot strategies, J. Appl. Physiol. 76, 965, 1994.

Williams, J. W., Jackson, S.T. and Kutzbach, J.E.: Projected distributions of novel and disappearing climates by 2100AD, Proc. Natl. Acad. Sci. U. S. A., 104, 5738– 5742, 2007.

Yang S., Gruber N., Long M. C., Vogt M.: ENSO-driven variability of denitrification. Global Biogeochemical Cycles, 31
655   (10), 1470–1487. doi: 10.1002/2016gb005596, 2017.

Zbilut, J. P. and Webber, C. L., Jr.: Embeddings and delays as derived from quantification of recurrence plots, Phys. Lett. A 171, 199, 1992.